Int. J. Heat Mass Transfer. Vol. 30, No. 3, pp. 479–496, 1987
Printed in Great Britain

0017–9310/87 $3.00 + 0.00

Effects of magnetically damped convection during the controlled solidification of metals and alloys

CHARLES VIVES and CHRISTIAN PERRY
Université d'Avignon, Laboratoire de Magnétohydrodynamique, 33 rue Louis Pasteur, 84000 Avignon, France

(*Received* 25 *March* 1986 *and in final form* 5 *June* 1986)

Abstract—The role of natural and damped convection during the thermally controlled solidification of tin and aluminium alloys in a toroidal mould was studied. The damped convection was caused by a stationary and uniform magnetic field parallel to the gravity field. Temperature measurements made it possible to follow both the evolution of the solidification front and that of the temperature distribution inside the bulk liquid with time. These experiments were performed from various degrees of superheat, in the absence and presence of a magnetic field. A discussion is presented relating the crystallographical findings to the temperature field patterns.

1. INTRODUCTION

OWING to the development of the semi-conductors and laser techniques, the production of solids constituted from a single crystal has become of primary importance and given rise to several methods of growing crystals, such as zone melting, floating zone melting, and Bridgeman and Czochralsky systems [1]. In the same way, an increasing interest has recently been shown in the application of stationary magnetic fields for controlling natural convection in crystal growth [1–5].

Over the last two decades, the role of heat transfer in solidification of metals and alloys has been partially studied in free convection [6–10], but only few investigators [2–5] have reported on the influence of stationary magnetic fields on the crystal structure during the solidification of alloys; it should be noted that, in these experimental works, the initial thermal boundary conditions were generally not accurately defined.

More recently, an interesting theoretical study, describing the fluid flow field and the temperature distribution in a rectangular cavity, in the presence of a horizontal and stationary magnetic field $\mathbf{B}_0$, has been presented by Oreper and Szekely [11]. In this problem a constant temperature difference was applied between two vertical opposite walls, while the upper and lower surface of the enclosure had a linear variation in temperature imposed upon them. The following assumptions were made in the statement of the problem: the magnetic field was both perpendicular to the hot and cold walls; the walls of the cavity were electrical insulators; and the flow was considered to be laminar. In ref. [11], where the solid–liquid phase change was not examined, it was found that the magnetic field can partially inhibit the natural convection; thus, for a sufficient strength $\mathbf{B}_0$, the temperature profiles in the system would become similar to those encountered for the case of a pure conduction mode.

In a recent paper [12] we have described the thermal and crystallographical effects of natural and forced convection during the controlled solidification of tin. The present work is devoted to the examination of the influence of a damped convection, caused by the application of a stationary magnetic field, and may be considered as the pursuit of an attempt at a comparative study of the heat and mass transfer phenomena, which occur during the crystallization of metals and alloys in the presence of natural, forced and damped convections.

In the present experimental work, the study of the effects of natural convection during the tin solidification has been extended to higher initial superheat ($\Delta T = 100°C$) and three representative cases of solidification were successively examined through the experimentation of a pure metal (tin) and of the 1050 and 2024 aluminium alloys, respectively characterized by a narrow and a wide freezing range (i.e. interval between liquidus and solidus temperature).

2. EXPERIMENTAL APPARATUS AND PROCEDURE

Both the procedure and the main features of the apparatus (Fig. 1) have already been detailed in a recent publication [12] to which we refer the reader. Consequently, we will confine ourselves to summarizing the principal characteristics of the device.

The apparatus consisted of a toroidal crucible, made of stainless-steel, containing about 2 dm^3 of molten metal with a free surface. The outer cylinder of 174 mm i.d. was resistance heated, while the inner cylinder of 24 or 42 mm o.d. (respectively, for the cases of tin and aluminium alloys) was internally cooled by water at 20°C, with a flow rate of 1000 $dm^3\,h^{-1}$. All the exterior walls of the furnace were thermally insulated.

NOMENCLATURE

$\mathbf{B}_0$	externally imposed magnetic field
b	induced magnetic field
c	specific heat
g	gravity
Gr	Grashof number, $g\beta\rho^2H^3\Delta T/\eta^2$
H	liquid metal height
J	induced current density
k	thermal conductivity
L_f	latent heat of fusion
M	Hartmann number, $B_0H(\sigma/\eta)^{1/2}$
M^2Re'/Gr	electromagnetic force/buoyancy force, $\sigma UB_0^2/\rho g\beta\Delta T$
M^2/Gr	(electromagnetic force) (viscous force)/(buoyancy force) (inertial force), $\eta\sigma B_0^2/\rho^2g\beta H\Delta T$
N	interaction parameter, M^2/Re'
Pr	Prandtl number, $\eta c/k$
r	radial position
Ra	Rayleigh number, $GrPr$
Re'	Reynolds number, $UH\rho/\eta$
R_i, R_e	inner and outer radius of the crucible
Ste	Stefan number, $c(T_0 - T_f)/L_f$
T_0	initial temperature of the bulk liquid
T_f	melting point
t	time
U	characteristic velocity, $(\nu/H)\sqrt{Gr}$
u	local velocity.

Greek symbols

α	thermal diffusivity
β	thermal expansion coefficient of liquid
ΔT	initial superheat
$\Delta T'$	superheat at a given time
ΔT^*	$\Delta T'/\Delta T$
η	viscosity
μ	magnetic permeability
ν	kinematic viscosity
ρ	density
σ	electric conductivity of liquid.

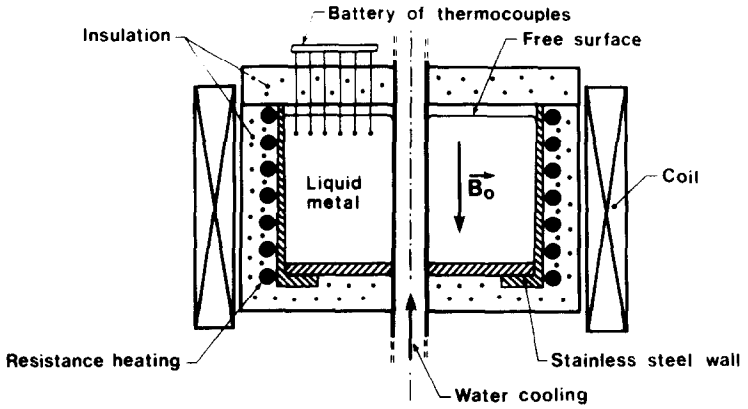

FIG. 1. Schematic diagram of the apparatus.

The damped convection was created by an externally imposed stationary magnetic field $\mathbf{B}_0$, parallel to the gravitational force field vector. This magnetic field, uniform to 2% inside the melt, was generated by an inductor made up of 248 jointed turns traversed by a direct current of 0–165 A, whereas the corresponding strength was included between 0–0.1 Tesla.

It should be noted that in these phenomena, the superheat, the melt volume, the boundary conditions and consequently the convective flow are time dependent. So, in order to follow both the evolution of the solidification front and of the temperature distribution inside the bulk liquid with time, six thermocouples were placed horizontally at prescribed heights within the melt (Fig. 1), their outputs being fed to a six-channel recorder. Each experiment was performed by melting the metal and heating it to 10°C above the required superheat temperature, at this moment the heating was cut off so that the liquid metal could cool slowly to the required superheat temperature T_0. Then, the ingots were solidified by delivering cooling water from an initial superheat of ΔT°C above either the melting point (tin), or the liquidus temperature (aluminium alloys).

3. SOLIDIFICATION OF COMMERCIALLY PURE TIN

3.1. *Natural convection*

In a recent work [12], we have considered the case of a low initial superheat ($\Delta T = 3$°C) and showed that the melt–solid interface was practically vertical during

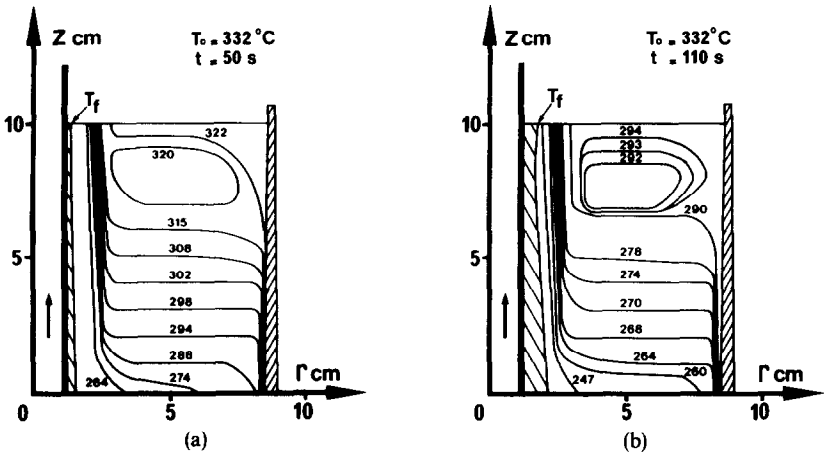

FIG. 2. Temperature fields in natural convection ($\Delta T = 100°C$): (a) $t = 50$ s; (b) $t = 110$ s.

the outward solidification. Moreover, on account of the low horizontal thermal gradients inside the bulk liquid, the natural convection is probably weak and laminar, so conduction is here the predominant mode of heat transfer. On the other hand, for a higher superheat ($\Delta T = 43°C$), the influence of the free convection increases and the fluid particles move upward along the hot wall and downward along the cold wall. Consequently, at the onset of freezing the solidification front is now inclined [7, 12], furthermore the hotter zone is situated in the vicinity of the free surface and the radial thermal gradients are steeper in the upper part than in the neighbourhood of the bottom of the solidifying melt.

The isotherm maps, presented in Fig. 2, correspond to a new set of experiments performed from a very high superheat of 100°C. Examination of the recordings shows the presence of strong fluctuations of temperature and reveals the occurrence of a turbulent convection, particularly located in the vicinity of the solidifying crust. Owing to the high values of the Grashof and Rayleigh numbers [12] the buoyancy-driven flows certainly play a dominant role. Figure 2(a), plotted for $t = 50$ s, shows the existence of an isothermal zone (320°C) situated in the upper part of the bulk liquid, the lower interior region being characterized by horizontal isothermals which are nearly uniformly spaced, indicating constant vertical temperature gradients. Moreover, the steepest radial gradients occur upward along the melt–solid interface and downward on the hot wall. The temperature field, plotted for $t = 110$ s, in Fig. 2(b), exhibits a similar trend to that already seen in Fig. 2(a), whereas the averaged superheat drop is 50°C for 110 s. Velocity measurements using an incorporated magnetic probe of 3 mm diameter [12–15] allowed the detection of a convective fluid motion, only in the proximity of the vertical walls, with peak velocities of about 4 cm s^{-1}, unfortunately it has not been possible to explore completely these zones on account of a probe–wall interaction effect: it should be mentioned that these

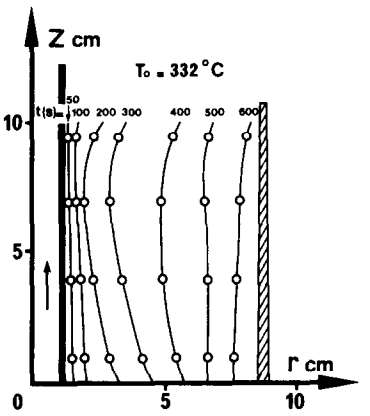

FIG. 3. Shape and position of the solid–liquid interface in natural convection ($\Delta T = 100°C$).

measurements are particularly difficult on account of the movement of the solidifying crust.

Figure 3 presents the evolution with time of the solid metal thickness (the solidification front position has been determined from an experimental procedure already described [7, 12]). In the early stages of freezing, the solidification front exhibits a concave shape which very probably coincides with the presence of a single convective loop; from $t = 500$ s this concavity vanishes gradually obviously because the thermal gradients and, consequently, the liquid movements are strongly attenuated.

Under this condition of very high superheat, the strong convective flow which appears at the initiation of the solidification may be considered as equivalent to a hydrodynamic stirring promoting the dissipation of superheat. Figure 4 shows a sketch depicting the dependence of the adimensional superheat ΔT^* on the dimensionless radius of the solidified crust (ΔT^* denotes the ratio of the superheat $\Delta T'$ at a given radius, or time, to the initial superheat ΔT and r^* is the ratio of the radius of the front at a given time to the radius at the end of solidification). Comparison

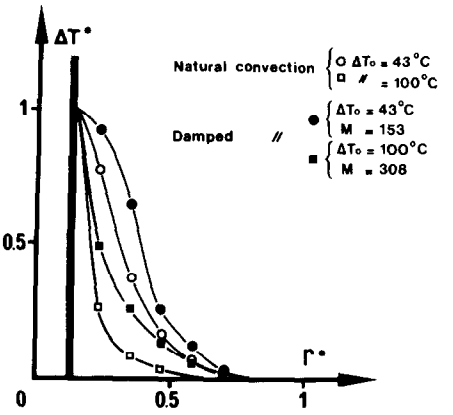

FIG. 4. Superheat drop as a function of the thickness of the solidifying crust (dimensionless parameters), in natural and damped convection, from different values of magnetic field and initial superheat.

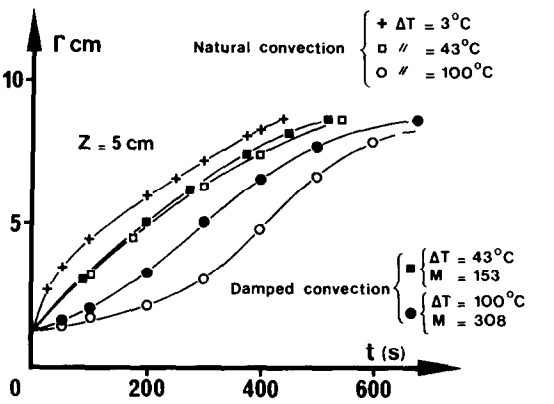

FIG. 5. Thickness of solid metal during solidification in natural and damped convection, from various values of magnetic field and initial superheat.

between experiments, carried out from 43 and 100°C of superheat (Fig. 4), confirms that the rate of evacuation of sensible heat increases considerably with the initial superheat, i.e. with the intensity of the convective flow.

During solidification, the metal liberates simultaneously sensible and latent heats, the high values of superheat promoting the superheat drop (Fig. 4), it is expected that the growing of the solidified portion should be slowed down under these circumstances [16, 17]. Figure 5 illustrates the evolution of the liquid–solid interface position with time and reveals, particularly at the onset of freezing, the dramatic effect of superheat on the solidification rate. As an example, a crust radius of 5 cm is reached after 120 s, for $\Delta T = 3°C$, and after 400 s, for $\Delta T = 100°C$.

3.2. *Solidification in the presence of a stationary magnetic field*

The system was immersed during the complete solidification in a stationary magnetic field, parallel to the gravity field (Fig. 1). In such problems, when the liquid metal is set in motion by the action of the buoyancy forces, an induced current of density **J** (caused by an induced e.m.f. due to the Lorentz law) arises. The externally imposed magnetic field $\mathbf{B}_0$ interacts with the induced current density **J** and gives rise to Lorentz forces which depend on the electromagnetic boundary conditions and are generally characterized by a tendency to damp out the liquid metal flows. The damping effect depends on an important dimensionless parameter: the Hartmann number, $M = B_0 H(\sigma/\eta)^{1/2}$, representing the square root of the ratio of the electromagnetic body force to the viscous force and where H, σ and η are, respectively, the liquid metal height, the electric conductivity and the viscosity of the bath. Another nondimensional number termed 'interaction parameter', $N = M^2/Re' = B_0^2 H\sigma/U\rho$ (where Re', U and ρ are respectively the Reynolds number, a characteristic velocity and the density of liquid), representing the ratio of the electromagnetic force to the inertial force, is also commonly used in magnetohydrodynamics [18].

Hence the molten metal is subjected both to the buoyancy forces (caused by the temperature gradients) and the Lorentz forces $\mathbf{J} \times \mathbf{B}$, with $\mathbf{B} = \mathbf{B}_0 + \mathbf{b}$, $\mathbf{b}$ being the induced magnetic field; in such problems [18] $\mathbf{b}$ is negligible with respect to $\mathbf{B}_0$. Therefore, it would be appropriate to add, for future and more comprehensive studies, other parameters taking into account the interaction between the thermal phenomena. For instance, combinations including the Grashof number ($Gr = g\beta\Delta T\rho^2 H^3/\eta^2$), such as $N \cdot Re'^2/Gr = M^2 \cdot Re'/Gr = \sigma U B_0^2/\rho g\beta\Delta T$, which is the ratio of the electromagnetic force to the buoyancy force, should be very useful. It should be mentioned that, in these liquid metal flows, the velocity is generally unknown and must be replaced by a characteristic velocity, such as $U = (\nu/H)\sqrt{Gr}$, for instance; however, this latter value seems overestimated, particularly for the cases of turbulent convection.

Another dimensionless group, $M^2/Gr = \eta\sigma B_0^2/\rho^2 g\beta H\Delta T$, offers the advantage of eliminating the velocity and extending the number of well-known parameters acting on the phenomena. Its physical significance is the ratio: (electromagnetic force) (viscous force)/(buoyancy force) (inertial force).

Lastly, because of the transient character of the phenomena and especially the decay of superheat with time, the relative influence of the electromagnetic forces increases during solidification in the mould.

The recordings presented in Figs. 6(b) and (c), dealing with an enhancement of the magnetic field strength, show a pronounced damping of the temperature oscillations seen in Fig. 6(a) and corresponding to the absence of magnetic field; the fluctuations are markedly subdued for $M = 85$ and removed for $M = 308$. Moreover, complementary experiments show that the temperature fluctuations are still suppressed for $M = 308$, even for a higher superheat of 100°C ($M^2\,Re/Gr = 1.93$).

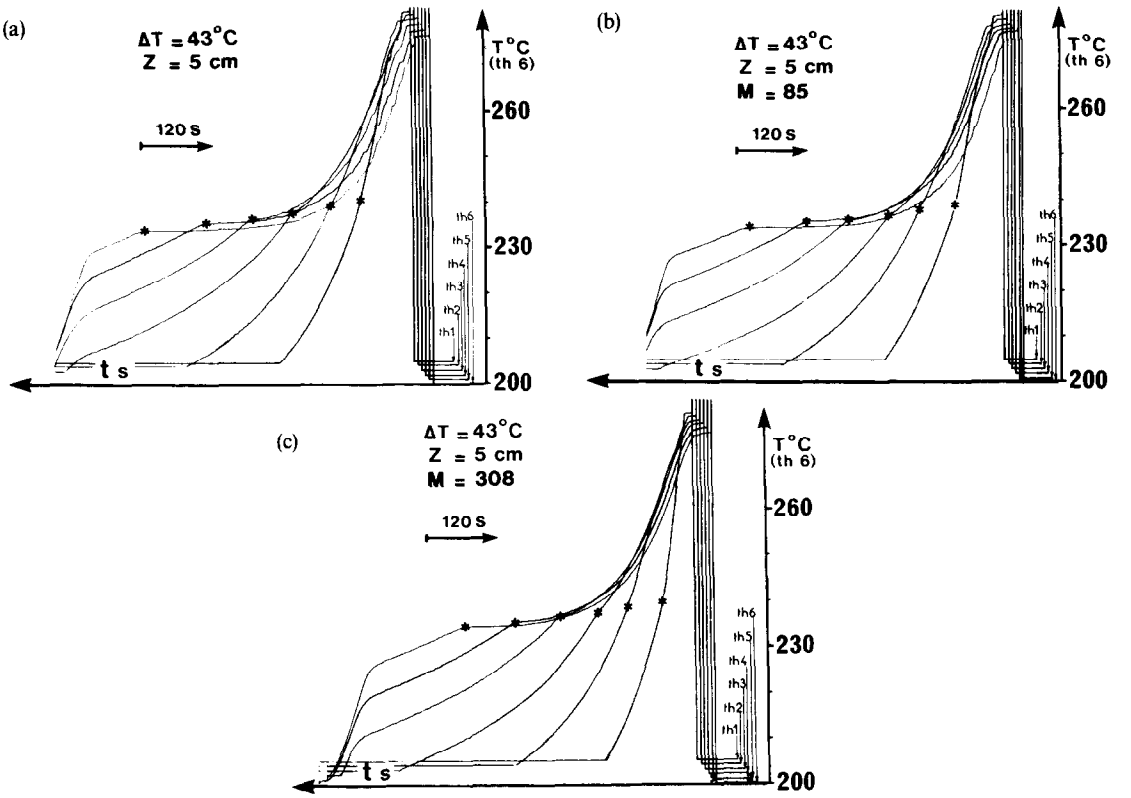

FIG. 6. Temperatures recorded at mid-height of the melt, from the same initial superheat, in natural convection (a) and in the presence of magnetic fields (b) $M = 85$, (c) $M = 308$.

Inspection of the temperature field sketched in Fig. 7(a) ($M^2 Re'/Gr = 0.84$) reveals clearly the occurrence of two different zones. The presence of horizontal isotherms, in the upper part of the core region, allows the expectation that the molten metal is practically stagnant inside this zone, while two typical thermal boundary layers, probably accompanied by a convective flow, and restricted to a peripheral layer adjacent to the vertical walls, appear. On the other hand, the low radial thermal gradients which exist in the lower part, particularly in the vicinity of the solidifying crust, indicate that conduction seems to be a substantial mechanism and that the velocities are probably very small in the bottom region. To summarize, a convective cell fills an upper zone corresponding to 2/3 of the volume occupied by the liquid metal, while the upper corner of the hot surface indicates a region where the flow starts.

Figure 7(b) presents a temperature field, plotted for $t = 110$ s; its inspection confirms the existence of the two zones already seen in Fig. 7(a). Comparison between Figs. 7(a) and (b) reveals that the superheat drop is more important in the upper part (of the order of 20°C, for 1 min) than in the proximity of the mould bottom (5–10°C, for the same duration). This latter remark corroborates the assumption expressed above about the velocity field within the tin pool.

Figure 7(c) shows an isotherm map plotted for $M^2 Re'/Gr = 1.93$ and characterized by both a very high superheat and a strong Hartmann number. Steep horizontal thermal gradients appear at the vertical walls in the upper region of the pool while the thickness of the boundary layer is found to increase downward along the solidifying crust. Moreover, the central region is isothermal in the horizontal direction, while the temperature of this core region was again found to decrease almost linearly in the vertical direction, from top to bottom. This temperature field pattern allows the prediction of a circulation of liquid metal concentrated within two thin boundary layers, located along the vertical walls. Hence, heat transfer takes place mainly by convection along the liquid–solid interface and by conduction inside the melt core region. Comparison between Figs. 7(c) and 2(a), which are characterized by both identical superheat and solidification time, shows that the application of magnetic field increases substantially the vertical thermal gradients; as an example, under the same circumstances, the temperature difference between top and bottom is 58°C, in natural convection [Fig. 2(a)], and 78°C, in the presence of a magnetic field [Fig. 7(c)].

Figure 7(d) (plotted for $t = 110$ s) shows that the trend of the isotherms is not considerably modified. Furthermore, it may be seen, with respect to Fig. 7(c), that the dissipation of superheat is significant in the bulk liquid, except in the left-hand side of the lowest zone of the melt. This latter finding may be understood by the fact that, in such a region, the isotherm shapes

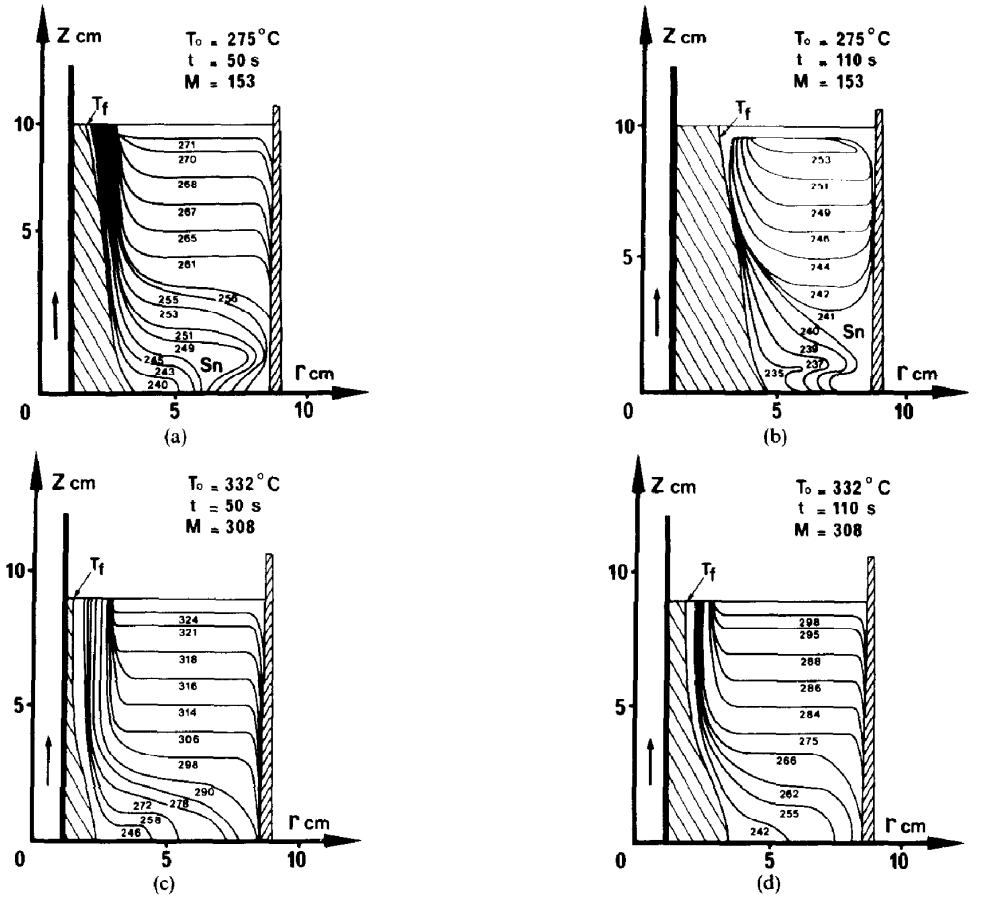

FIG. 7. Temperature fields plotted in the presence of magnetic fields: (a) $\Delta T = 43°C$, $M = 153$, $t = 50$ s; (b) $\Delta T = 43°C$, $M = 153$, $t = 110$ s; (c) $\Delta T = 100°C$, $M = 308$, $t = 50$ s; (d) $\Delta T = 100°C$, $M = 308$, $t = 110$ s.

and the rapid diminution of the thermal gradients are typical of the predominance of a conductive mode of heat transfer with respect to the convective one.

The marked inclination of the solidification front showed in Fig. 8, until a solidification time of 400 s, reveals that the thermal transfers are again two-dimensional. Consequently, the heat transfer being not exclusively conductive, the magnetic field may be unable to inhibit totally fluid motion, even for high values of the Hartmann number ($M = 308$). This remark is qualitatively in accordance with the finding recently presented by Oreper and Szekely in a theoretical work [11] concerning the schematic representation of physical phenomena in crystal growth in the presence of a magnetic field. However, it must be mentioned that, in this latter study and notwithstanding some similarities, the electromagnetic and thermal boundary conditions, as well as the orientation of the magnetic field (perpendicular to the gravity field), were different from those of the present experimental device.

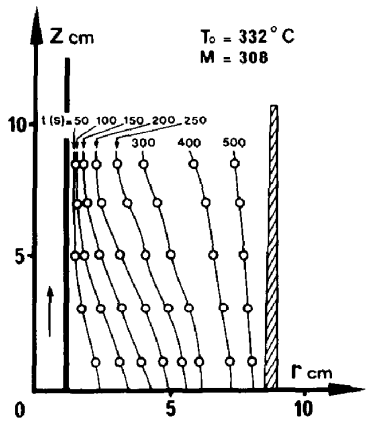

FIG. 8. Shape and position of the solid–liquid interface ($\Delta T = 100°C$, $M = 308$).

Figure 4 shows that, whatever the initial superheat, the withdrawal of heat is markedly delayed by the application of the magnetic field. This effect is most likely provoked by a pronounced damping of the convective liquid metal flows in the central region of the pool.

The rate of movement of the interface is significantly accelerated for $M^2Re'/Gr = 1.93$, but only slightly increased for $M^2Re'/Gr = 0.84$ (Fig. 5). This observation is again consistent with the interpretation already expressed in the case of natural convection for various values of the initial superheat (Section 3.1, Fig. 5): the superheat drop is retarded to the profit of the liberation of latent heat.

4. SOLIDIFICATION OF ALUMINIUM ALLOYS

4.1. *Natural convection*

The experimental materials were, first, a 1050 aluminium alloy (Al, 99.5% and traces of Si, Fe, Cu, Mn, Mg, Zn and Ti; liquidus: 664°C, solidus: 635°C) and, second, a 2024 aluminium alloy (Al, 92.2%; Cu, 4.2%; Mg, 1.6%; Si, 0.5%; Fe, 0.5%; Mn, 0.7%; Ti, 0.15%; other impurities, 0.15%; liquidus: 645°C; solidus: 485°C). The initial superheat was, in any case, 35°C above the liquidus temperature.

4.1.1. *Solidification of the* 1050 *aluminium alloy.* The temperature field, displayed in Fig. 9(a), presents some similarities with the one already seen in Fig. 7(a) corresponding to the solidification of tin in the presence of a magnetic field. Two thermal boundary layers appear at the vertical walls and these layers are thin compared to the width of the cavity, being separated by an isothermal portion in the temperature profiles, while the steepest gradients occur both in the upper-left and the lower-right corners. Inspection of Figs. 9(b) and (c) reveals the rapid diminution of the radial and vertical gradients; the result is that 1 min after the freezing starts (i.e. when only about 8% of the melt has been solidified), the thermal phenomena are characterized by a transition state lying between the conduction regime and the boundary layer regime.

4.1.2. *Solidification of the* 2024 *aluminium alloy.* Experiments show that the transition from the fully liquid state to the liquidus isotherm is clearly revealed by the sudden change of slope of recordings, while the passage from the solidus isotherm to the solid state takes place continuously. On the other hand, complementary experiments showed that the two-phase medium localized within the mushy zone behaves, from the consistency standpoint, practically as a solid when the temperature of the bath is 3°C below the liquidus temperature, dealing with an amount of 13% of suspended solid particles into the melt. Consequently, the shape of the solidifying crust may be rather properly represented by the liquidus profile.

Figure 9(d) depicts a temperature field plotted at the onset of solidification, comparison with Fig. 9(a), which displays an isotherm map sketched under identical circumstances ($\Delta T = 35°C$, $t = 15$ s), indicates that the heat flow behaviour of the 1050 and 2024 alloys are radically different. Actually, it is necessary to know the appropriate physical properties of these alloys, unfortunately their constants could not be found in the literature. So the properties of pure aluminium, presented in Table 2, must very likely be considered as crude order-of-magnitude estimates (especially for the 2024 aluminium, which contains a large amount of alloying elements).

With regard to Fig. 9(a), it is seen from Fig. 9(d) that the radial and, mainly, the vertical isothermal gradients are now markedly decreased. The thickness of the thermal boundary layers increases and it follows that the convective effects are subdued. Consequently, in the fully liquid zone, heat is transferred both by conduction and convection, mostly by the former. Moreover, and in contrast to the case of a pure metal, heat flow is primarily transported by conduction in the immediate vicinity of the solidification front (i.e. in the solidifying liquid–solid region), because the velocities are undoubtedly very weak, on account of the high values of the apparent viscosity in this area. Figures 9(e) and (f) reveal the gradual enhancement of the comparative contribution of the conductive mode during the phase change, which must be explained by the superheat drop.

The evolution of superheat with the average radius of the interface is illustrated in Fig. 10, where it is seen that superheat completely vanishes when the metallic mass is half-solidified (i.e. after the first quarter of the total freezing duration). It should be emphasized that the complete disappearance of superheat does not necessarily involve a breakdown of natural convection; in fact transient convection currents may persist in the system after the attainment of uniform temperature, until the final stages of solidification [11]. Moreover, the withdrawal of superheat is more rapid for the 1050 alloy than for the 2024 alloy. This finding is consistent with the remarks expressed earlier: the convective stirring being strongest for the case of the 1050 alloy promotes the evacuation of superheat. The different thermal behaviour of these alloys has repercussions on their solidification rate. Inspection of Fig. 11 confirms that the slower the superheat drop, the higher is the solidification rate; for example, a crust radius of 8 cm is reached after 140 s for the 2024 alloy, and only after 400 s for the 1050 alloy.

4.2. *Solidification in the presence of a stationary magnetic field*

4.2.1. *Solidification of the* 1050 *aluminium alloy.* The temperature field, presented in Fig. 12(a), reveals the presence of a hotter region in the upper-left-hand side corner. Furthermore, with respect to Fig. 9(a), it is seen that the thickness of the thermal boundary layers increases significantly, particularly in the vicinity of the solidifying crust. On the other hand, the horizontal isotherms—shown in Fig. 9(a)—are now markedly inclined, resulting in the vertical thermal gradients being noticeably reduced.

A linear temperature variation in the core region is seen in Figs. 12(b) and (c), the slope of these isotherms, defined with respect to the vertical direction, decreasing as the global superheat diminishes. This evolution of the isotherm maps is obviously connected with the gradual attenuation of the convective mode of heat transfer, mostly caused by the damping effect of the magnetic field.

4.2.2. *Solidification of the* 2024 *aluminium alloy.* Figures 12(d)–(f) convey temperature fields plotted at a given time. The nearly vertical shape of the isotherms

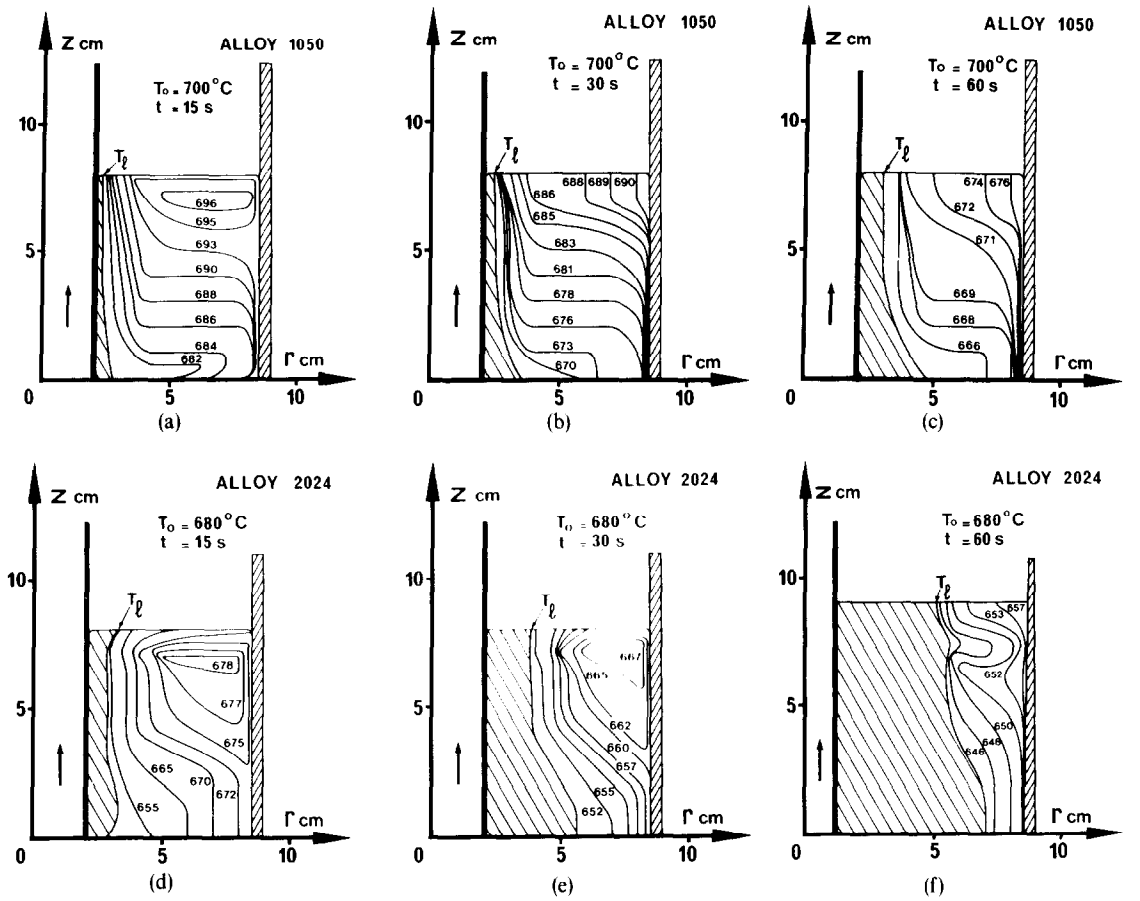

FIG. 9. Evolution of isotherm maps with time in natural convection: (a)–(c) 1050 aluminium alloy; (d)–(f) 2024 aluminium alloy.

Table 1. Thermophysical properties of pure aluminium

ρ	density	kg m^{-3}	2.38×10^3
η	viscosity	kg m^{-1} s^{-1}	2.90×10^{-3}
ν	kinematic viscosity	m^2 s^{-1}	1.22×10^{-6}
β	thermal expansion coefficient	K^{-1}	1.16×10^{-4}
σ	electric conductivity	Ω^{-1} m^{-1}	4×10^6
c	specific heat	J kg^{-1} K^{-1}	1.08×10^3
k	thermal conductivity	W m^{-1} K^{-1}	1.03×10^2
L_f	latent heat of fusion	J kg^{-1}	4×10^5
Pr	Prandtl number		3×10^{-2}
Gr	Grashof number ($\Delta T = 35$°C)		2.68×10^9
Ra	Rayleigh number ($\Delta T = 35$°C)		8×10^7
Ste	Stefan number ($\Delta T = 35$°C)		0.1

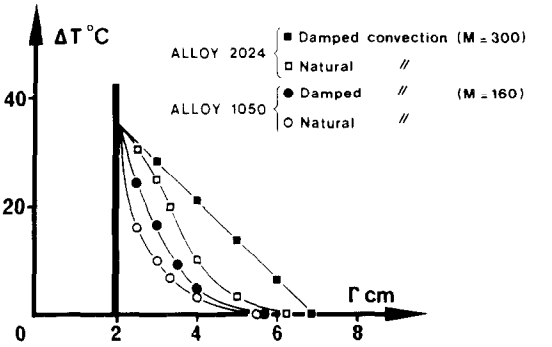

FIG. 10. Superheat drop as a function of the thickness of the solidifying crust, in the absence and presence of a stationary magnetic field (1050 and 2024 aluminium alloys).

is here typical of the predominance of a radial conductive heat flux. However, it has been theoretically predicted [11] that transient free convection is not necessarily completely suppressed, even when the isotherms are rigorously vertical, so it is not excluded that a weak laminar convective flow persists under such circumstances. Comparisons between Figs. 9 and 12 dealing with the 2024 alloy, show that the profile of the solidifying crust is noticeably affected by the presence of the magnetic field, particularly in the lower half of the mould where the truncated cone-shaped interface [Figs. 9(c) and (f)] is replaced by a cylindrical solidification front [Figs. 12(e) and (f)].

Figure 10 shows that, from the standpoint of the decline of superheat, the behaviour of these two specific alloys is similar to that of a pure metal, i.e. the withdrawal of superheat is markedly retarded by the application of a stationary magnetic field, mainly for the case of the 2024 alloy. Finally, the freezing rate is substantially enhanced by the presence of $\mathbf{B}_0$ (Fig. 11), which once again favours the evacuation of latent heat to the prejudice of superheat.

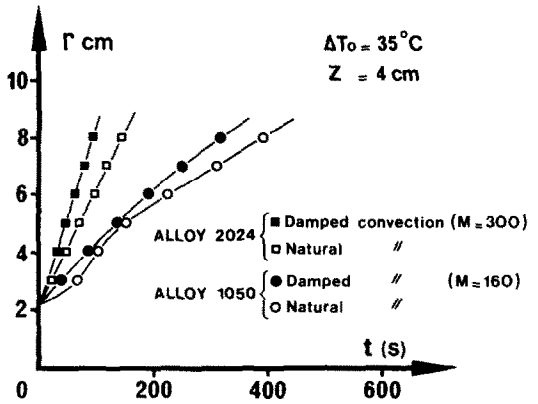

FIG. 11. Thickness of solid metal during solidification, in the absence and presence of a stationary magnetic field (1050 and 2024 aluminium alloys).

5. METALLOGRAPHIC STUDY AND DISCUSSION

The macrostructures of the materials investigated have been revealed in order to provide information on variation in structure, such as grain size, columnar and equiaxed crystals and even on the fluid flow patterns. Slices of about 15 mm thickness and 100 mm height were cut along whole radial and vertical cross-sections of the annular ingots. To this end, the ingots were sectioned, mechanically polished and then immersed into specific etching solutions [19]. In all cases, the left- and right-hand sides of the samples presented here, are respectively connected with the cold and hot wall of the mould.

5.1. *Commercially pure tin*

5.1.1. *Natural convection.* The presence of a unicellular liquid metal flow, with fluid rising near the hot wall and descending near the cold one, has been pointed out in a recent work [12]; it has also been shown that the columnar zone is sloped in the upstream direction to the interface [12, 20] and that the inclination of the dendrites increases with the degrees of superheat [Figs. 13(a)–(c)], mainly at the initiation of solidification.

5.1.2. *Magnetically damped convection.* The macrostructure presented in Fig. 13(d) has been yielded from a superheat of 3°C and a magnetic field of 0.09 T ($M^2\,Re'/Gr = 11.5$). The existence of two large single crystals displays the spectacular effect of the magnetic field on the crystal growth; with respect to the case of Fig. 13(a), the crystal volumes are multiplied by about 100.

Examination of Fig. 13(e) ($\Delta T = 43$°C, $B_0 = 0.09$ T, $M^2\,Re'/Gr = 2.96$) corroborates the finding, reported in Section 3.2; after inspection of the temperature field sketched in Fig. 7(a) the inclination of the columns,

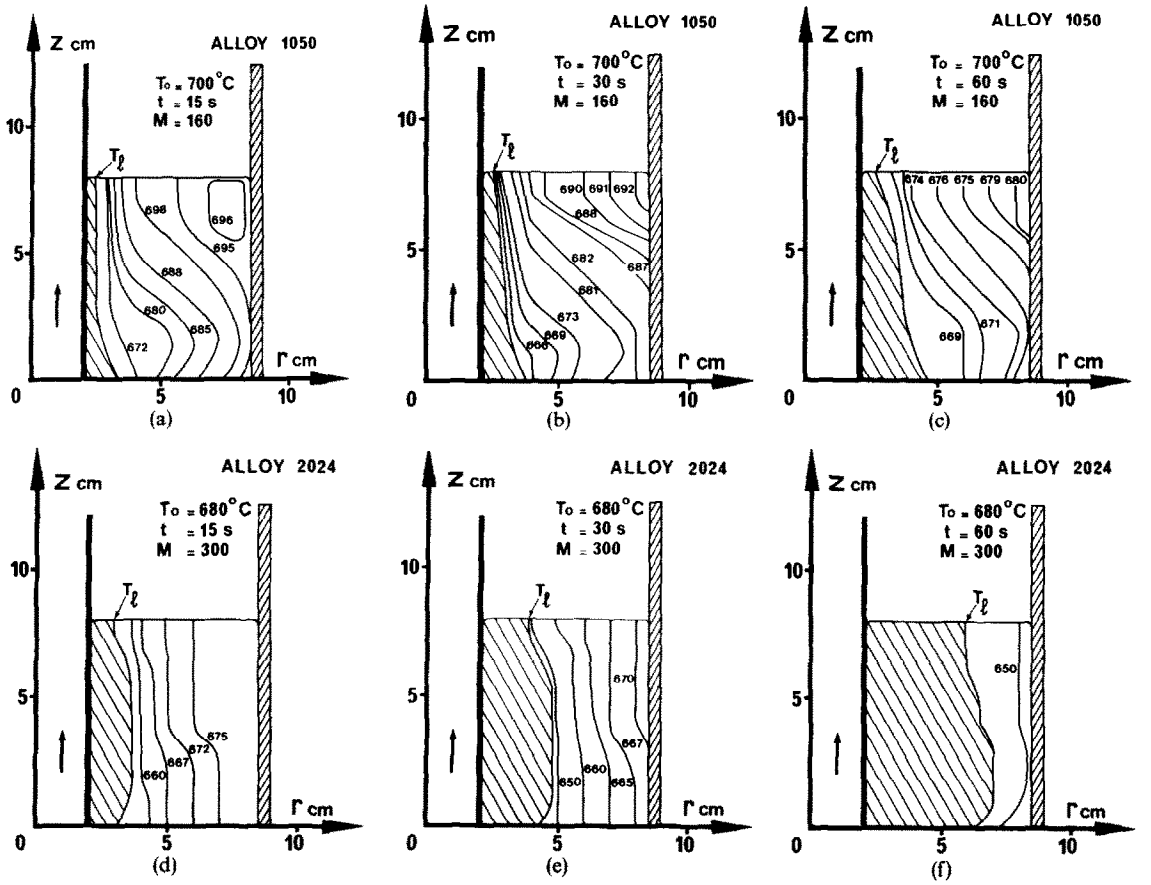

FIG. 12. Evolution of isotherm maps with time in the presence of a stationary magnetic field: (a)–(c) 1050 aluminium alloy; (d)–(f) 2024 aluminium alloy.

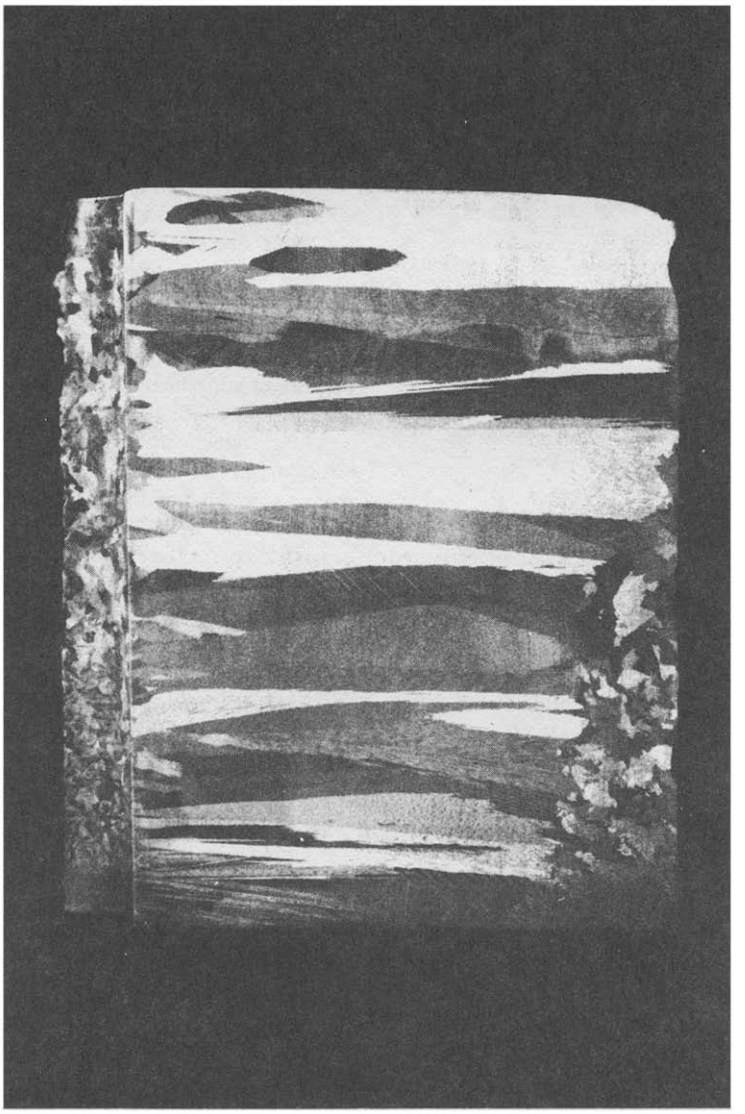

(a)

FIG. 13. Macrostructures of commercially pure tin solidified in natural convection: (a) $\Delta T = 3°C$; (b) $\Delta T = 43°C$; (c) $\Delta T = 100°C$, and in the presence of a stationary magnetic field: (d) $\Delta T = 3°C$, $M^2 Re/Gr = 11.5$; (e) $\Delta T = 43°C$, $M^2 Re/Gr = 2.96$; (f) $\Delta T = 100°C$, $M^2 Re/Gr = 1.93$.

in the upper part of the ingot, indicates that a convection motion continues to exist and, on the other hand, the radial growth direction of the crystals, in the lower part, proves that the movements of molten metal along the interface are very weak in this latter region. Moreover, the crystal sizes are still slightly enlarged, principally in the bottom area.

The sample displayed in Fig. 13(f) has been obtained from a superheat of 100°C ($B_0 = 0.9$ T, $M^2 Re'/Gr = 1.93$). By comparison between Figs. 13(c) and (f), it appears that the average diameter of the columnar crystals is slightly reduced at the onset of solidification and then enhanced during the latter stages of freezing; moreover, in the area relating to the beginning of solidification, the angle of inclination of the dendrites (defined with respect to the horizontal), increases from about 30° (without magnetic field) to 45° (with magnetic field). At first glance, these observations, confirmed by repetitive tests, may appear surprising and seem to signify that the convective stirring is here intensified, during the early stages of cooling, by the presence of a stationary magnetic field, at least in the near proximity of the melt–solid interface. An assumption may be advanced: under these particular circumstances, it is possible that the magnetic field provokes a relaminarization of the convective liquid metal flow (confined inside thin boundary layers adjacent to the walls and particularly to the solidification front), which is undoubtedly strongly turbulent for this case of free convection ($Gr = 2.96 \times 10^9$, $Ra = 3.4 \times 10^7$), Hence, for this relatively high value of superheat, the velocities may be increased on

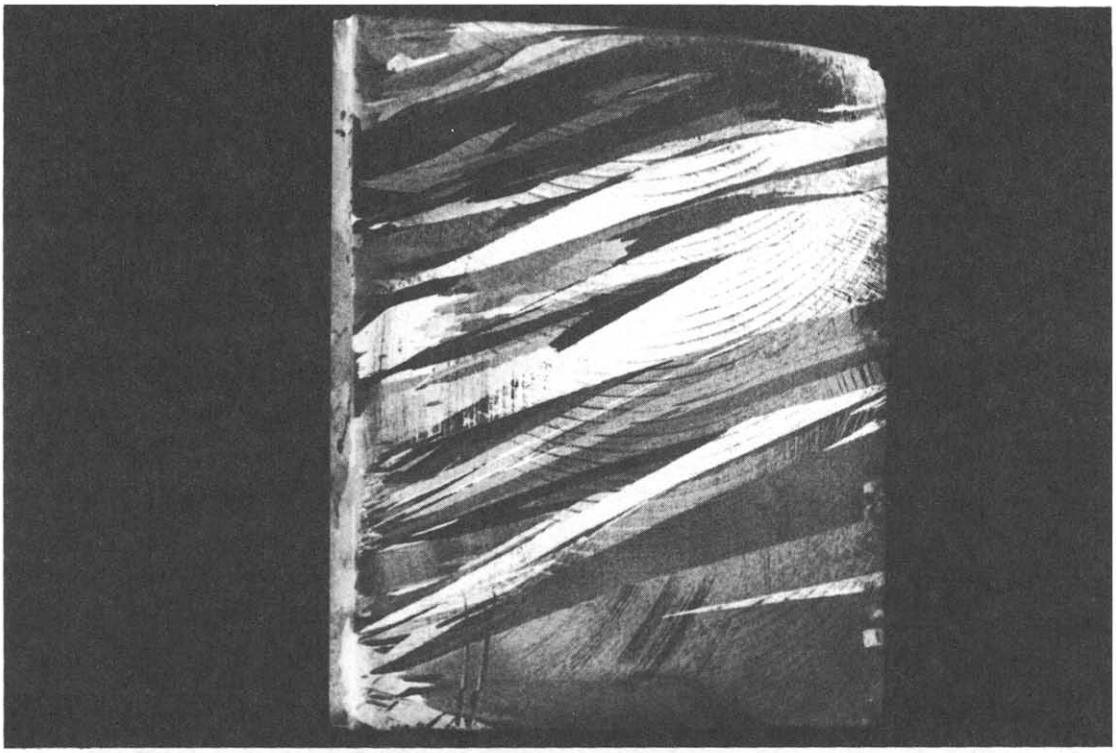

FIG. 13(b).

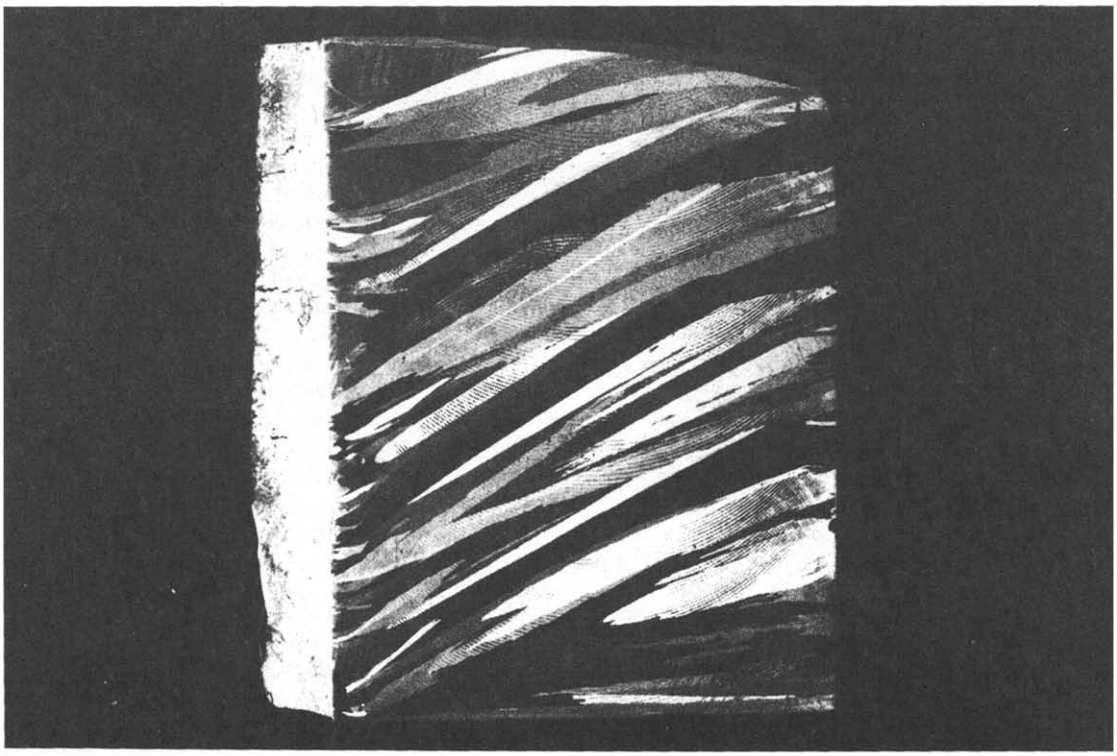

FIG. 13(c).

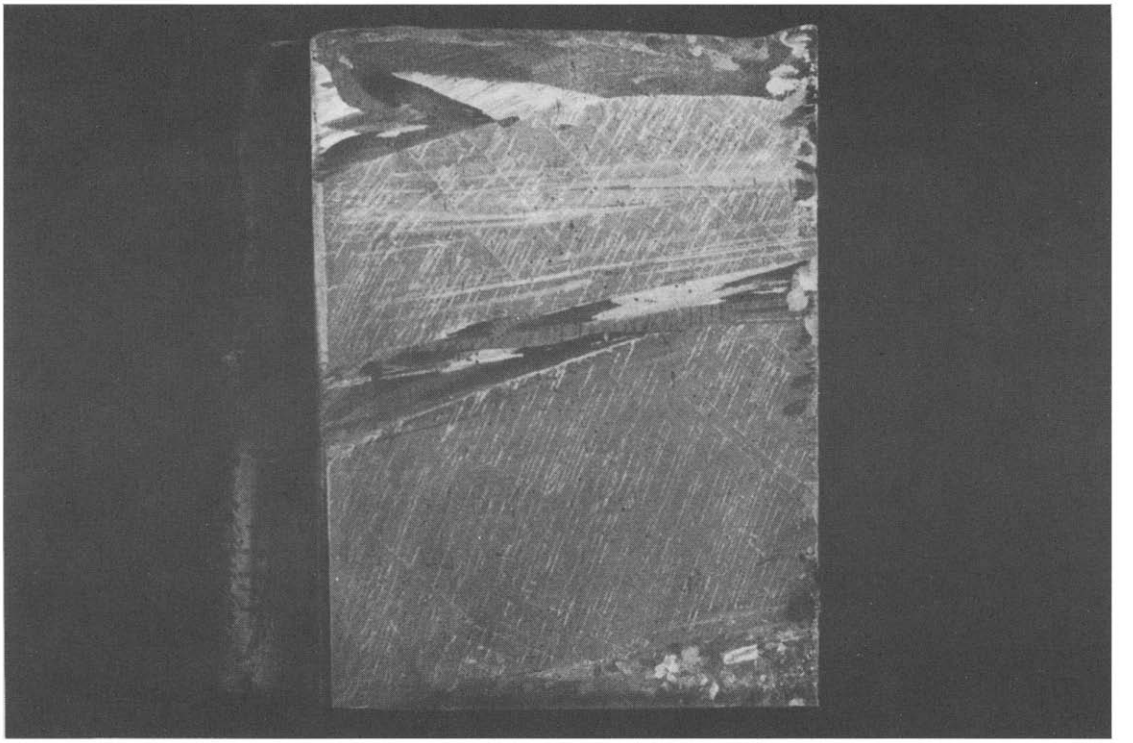

FIG. 13(d)

account of the passage from a turbulent state to a transition, or a laminar, state. This presumption is supported by the fact that, for this high degree of initial superheat, the solidification front is more inclined during the phase change in the presence of magnetic field (Fig. 8), than in natural convection (Fig. 3). Thus, the natural convection would be enhanced within the boundary layers and cancelled in the bulk liquid; however, from the thermal point of view, the overall effect results in a delayed withdrawal of superheat (Fig. 10). In fact, more extensive and delicate data would be required to elucidate the appropriate mechanisms responsible for this unexpected phenomenon.

Nevertheless, it is obvious that the ratio of the electromagnetic force to the buoyancy force ($M^2\,Re'/Gr = 1.93$) is here insufficient to damp out the convective movements in the vicinity of the solidifying crust and, consequently, to permit the production of large single crystals. To achieve this aim it would have been necessary to operate with experimental conditions corresponding to $M^2\,Re'/Gr \simeq 10$, hence, with a stronger magnetic field, of the order of 0.22 T; unfortunately, although this value should be rather moderate, our facilities do not allow such a strength to be attained.

5.2. *Aluminium alloys*

5.2.1. *Natural convection.* Inspection of vertical slices, solidified from an initial superheat of 35°C above the liquidus temperature and cut from ingots of 1050 aluminium alloy, shows that the crystallization is exclusively columnar. Moreover, on account of the existence of a convective flow, the dendrites are again oriented upstream and their average inclination, with respect to the horizontal, is about 18°. The sample, presented in Fig. 14(a), corresponds to a horizontal slice of 170 mm o.d., cut at the mid-height of the ingot and shows the sections of the oblique columns.

The macrostructure displayed in Fig. 15(a) was obtained from a 9-cm-high ingot of 2024 aluminium alloy ($\Delta T = 35$°C). The crystallization of this material corresponds to the typical structure of alloys characterized by a wide freezing range and involving, successively from the cold to the hot wall, chill and columnar zones (about 15 mm thick), followed by an equiaxed region. The marked behaviour difference between the 1050 and 2024 alloys has been revealed in the course of the thermal study; as an example, for the same flow rate of cooling water, the 2024 alloy is solidified three times more rapidly than the 1050 alloy (Fig. 11). It appears that this pronounced disparity subsists from the crystallization standpoint.

5.2.2. *Solidification in the presence of a stationary magnetic field.* The horizontal slice of 1050 aluminium alloy, obtained under the thermal conditions imposed in Fig. 14(a) and in the presence of a magnetic field of 0.09 T ($M^2\,Re/Gr = 5.4$), shows an outstanding example of unidirectional solidification [Fig. 14(b)].

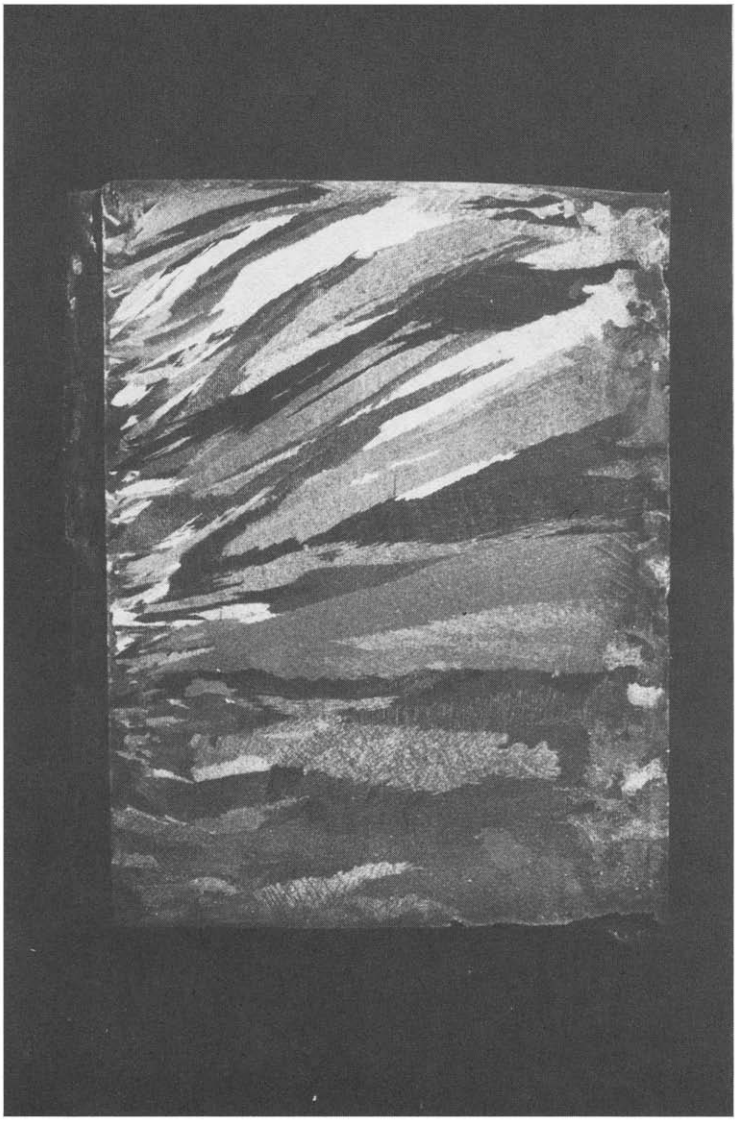

FIG. 13(e).

FIG. 13(f).

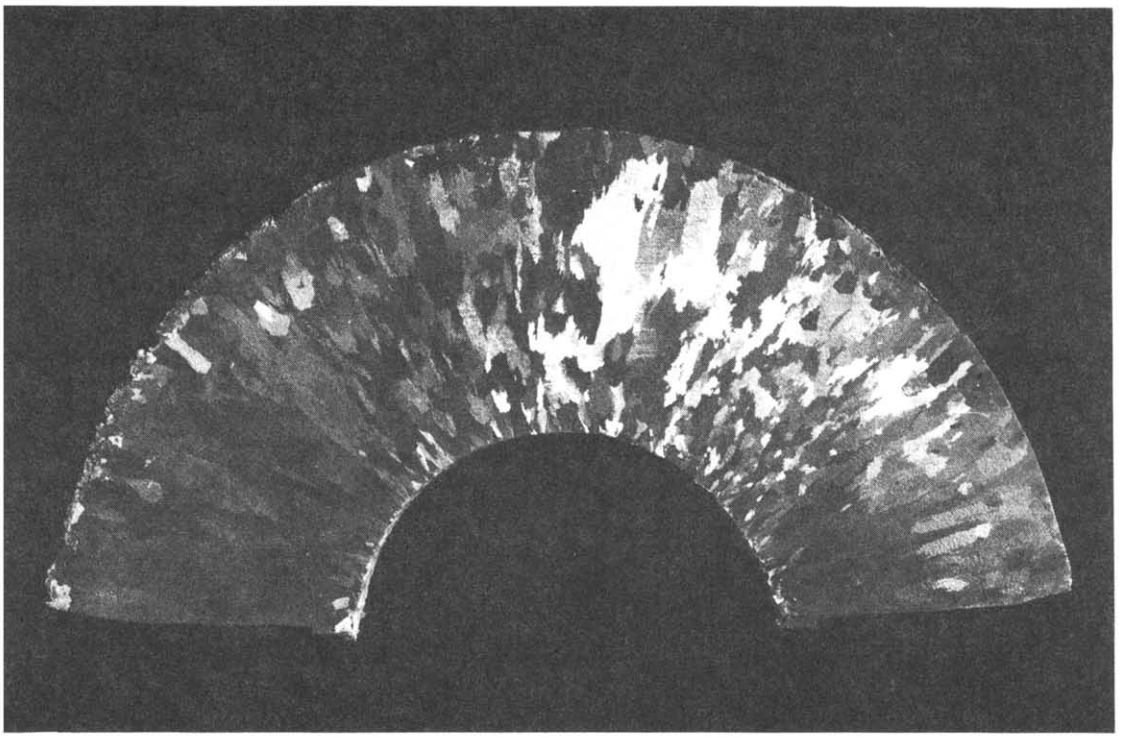

(a)

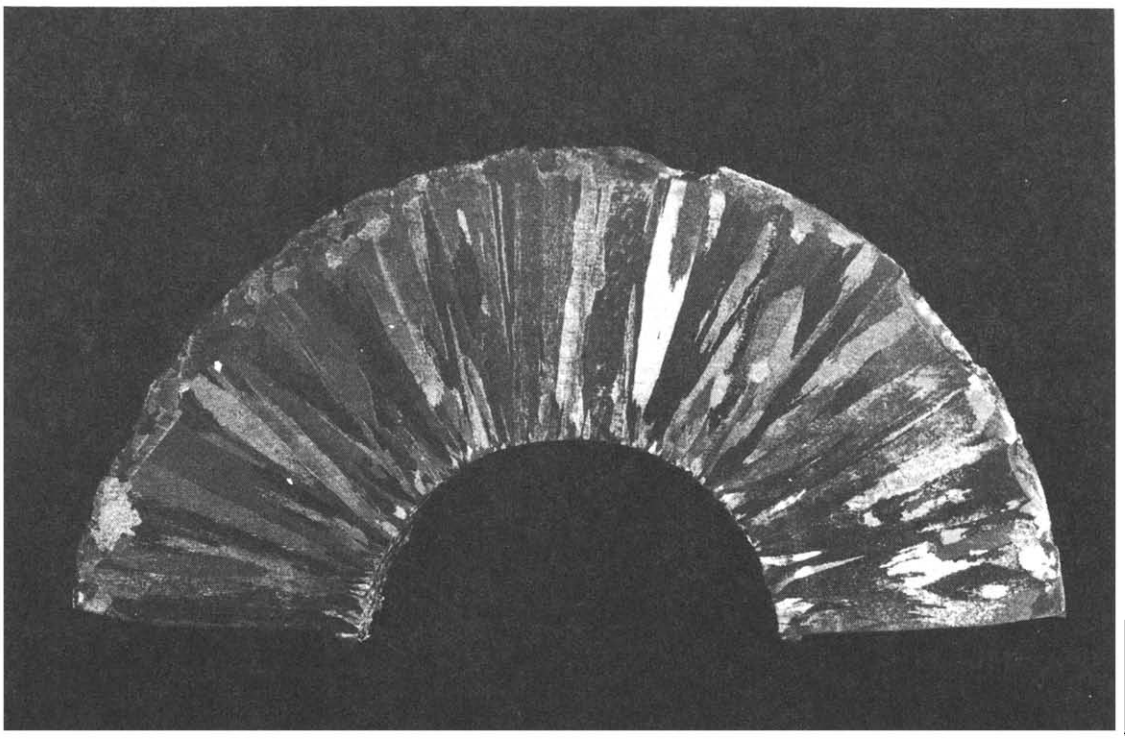

(b)

FIG. 14. Macrostructures of a 1050 aluminium alloy solidified: (a) in natural convection, $\Delta T = 35°C$; (b) in the presence of a stationary magnetic field, $M^2\,Re/Gr = 5.4$.

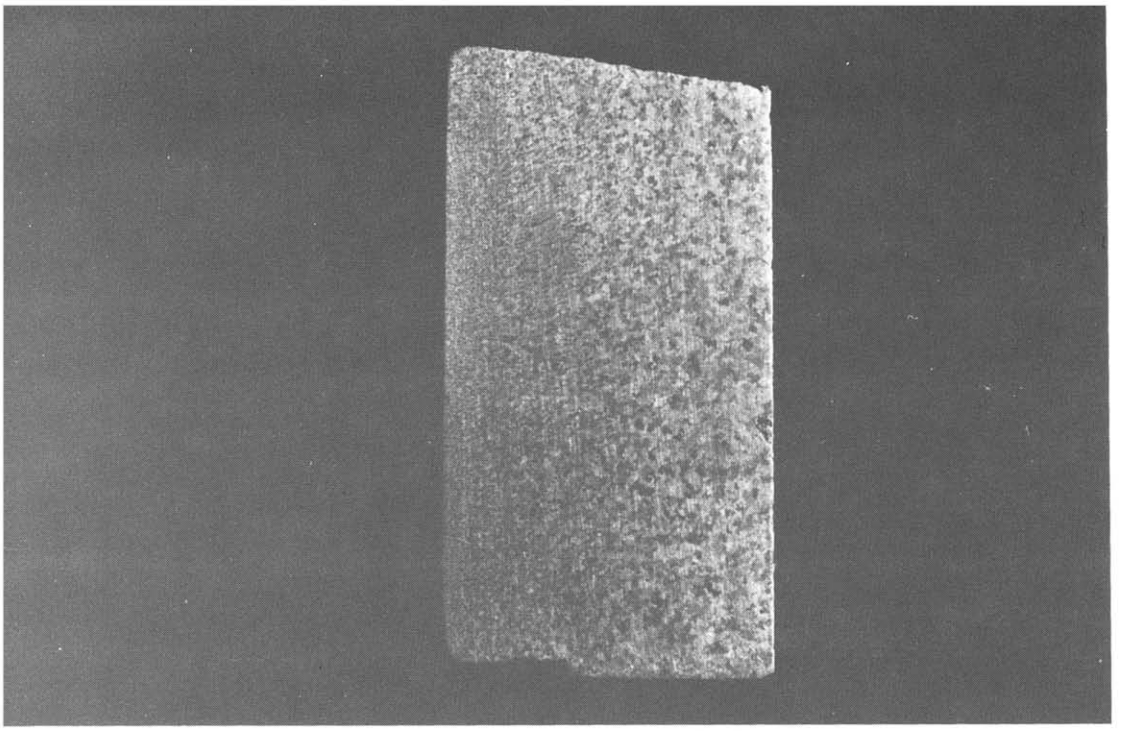

(a)

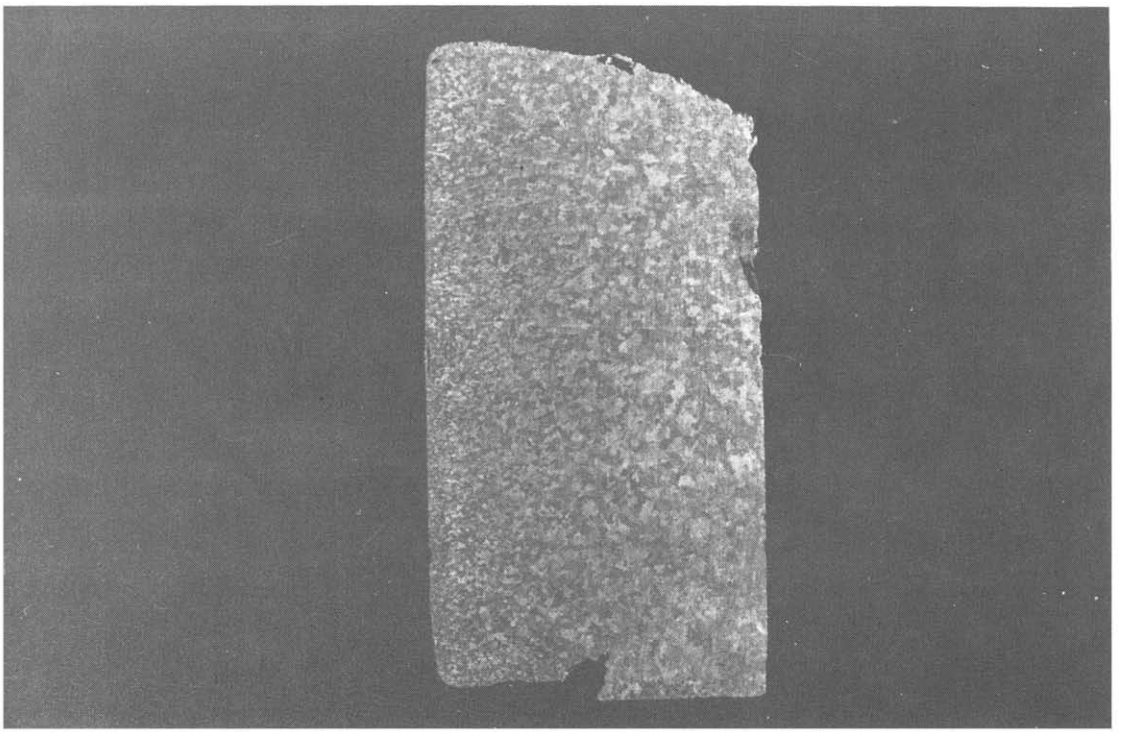

(b)

FIG. 15. Macrostructures of a 2024 aluminium alloy solidified: (a) in natural convection, $\Delta T = 35°C$; (b) in the presence of a stationary magnetic field, $M^2 Re/Gr = 5.4$.

The crystal growth is radial, showing that the free convection is here considerably damped by the magnetic field. Furthermore, the average diameter of the columns increases slightly, by about 30%.

Finally, for the case of the 2024 alloy and a magnetic field of 0.09 T [Fig. 15(b)], the number of crystals is divided by about 3, throughout the cross-section.

6. CONCLUSIONS

The role of natural and damped convection, caused by a magnetic field, during the solidification of tin and aluminium alloys in an annular mould were compared. The evolution of the thermal phenomena with time (or with the position of the solidification front) and also their interactions on the crystal growth were examined, for various degrees of superheat, both in the absence and presence of an axial and a stationary magnetic field.

In spite of the various values of the thermophysical properties and, consequently, of the very different thermal behaviour of the investigated materials, it occurs that, in any case, the effects of a stationary magnetic field during the solidification are principally characterized by a decrease of escape of superheat and an acceleration of the solidification rate, particularly at the initiation of phase change. Moreover, the adimensional groups, $M^2 Re'/Gr$ and M^2/Gr, seem more proper to represent the influence of the parameters which interact in such phenomena, involving magnetically damped thermal convection, than the classical Hartmann number.

Finally, the size of the columnar and equiaxed crystals are as much enlarged as the groups $M^2 Re'/Gr$, or M^2/Gr, are higher; furthermore, directionally solidified, or large, single crystals can be produced both from an adequate rate of heat extraction and through the use of stationary magnetic fields of sufficient strength.

Acknowledgements—The authors wish to thank the Conseil Regional Provence-Alpes-Côte d'Azur for financial support of this work.

REFERENCES

1. B. R. Pamplin, *Crystal Growth*. Pergamon Press, Oxford (1980).
2. U. P. Utech and M. C. Flemings, Elimination of solute banding in indian antimonide crystals by growth in a magnetic field, *J. appl. Phys.* **5**, 2021–2024 (1966).
3. D. R. Uhlmann, T. P. Seward and B. Chalmers, The effect of magnetic fields on the structure of metal alloy castings, *Trans. Met. Soc.* **236**, 527–531 (1966).
4. K. Hoshikawa, Czochralsky silicon crystal growth in the vertical magnetic field, *Japan. J. appl. Phys.* **9**, 545–547 (1982).
5. W. E. Langlois and Ki-Jun Lee, Czochralski crystal growth in an axial magnetic field: effects of joule heating, *J. Cryst. Growth* **62**, 481–486 (1983).
6. D. B. Spalding and N. H. Afgan, *Heat and Mass Transfer in Metallurgical Systems*. McGraw-Hill, New York (1981).
7. J. Szekely and P. S. Chhabra, The effect of natural convection on the shape and movement of the melt–solid interface in the controlled solidification of lead, *Met. Trans.* **1**, 1195–1203 (1970).
8. A. W. Hills, S. L. Malhotra and M. R. Moore, The solidification of pure metals (and eutectics) under unidirectional heat flow conditions: II. Solidification in the presence of superheat, *Met. Trans.* **B6**, 131–142 (1975).
9. C. Gau and R. Viskanta, Melting solidification of a metal system in a rectangular cavity, *Int. J. Heat Mass Transfer* **27**, 113–123 (1984).
10. C. Gau and R. Viskanta, Effect of natural convection on solidification from above and melting from below of a pure metal, *Int. J. Heat Mass Transfer* **28**, 573–587 (1985).
11. G. M. Oreper and J. Szekely, The effect of an externally imposed magnetic field on buoyancy driven flow in a rectangular cavity, *J. Cryst. Growth* **64**, 505–515 (1983).
12. Ch. Vivès and Ch. Perry, Effects of electromagnetic stirring during the controlled solidification of tin, *Int. J. Heat Mass Transfer* **29**, 21–33 (1986).
13. R. Ricou and Ch.Vivès, Local velocity and mass transfer measurements in molten metals using an incorporated magnet probe, *Int. J. Heat Mass Transfer* **25**, 1579–1588 (1982).
14. J. L. Meyer, F. Durand, R. Ricou and Ch. Vivès, Steady flow of liquid aluminum in a rectangular-vertical ingot mold, thermally or electromagnetically activated, *Met. Trans.* **B3**, 471–478 (1984).
15. H. C. Lee, J. W. Evans and Ch. Vivès, Velocity measurement in Wood's metal using an incorporated magnet probe, *Met. Trans.* **B4**, 734–736 (1984).
16. B. Chalmers, *Principle of Solidification*, p. 240. Krieger, Malabar, FL (1982).
17. M. C. Flemings, *Solidification Processing*, p. 19. McGraw-Hill, New York (1974).
18. J. A. Shercliff, *A Textbook of Magnetohydrodynamics*. Pergamon Press, Oxford (1965).
19. *Annual Book of A.S.T.M. Standards*, Section 3. American Society for Testing and Materials, Philadelphia (1983).
20. T. Takahashi, K. Ichikawa and M. Kudou, *Solidification and Casting of Metals*, pp. 331–342. Metals Society, Sheffield (1977).

EFFETS D'UNE CONVECTION AMORTIE ELECTROMAGNETIQUEMENT DURANT LA SOLIDIFICATION CONTROLEE DES METAUX ET ALLIAGES

Résumé—On étudie le rôle des convections naturelle et amortie durant la solidification controlée de l'étain et d'alliages d'aluminium dans un moule toroïdal. La convection amortie est provoquée par un champ magnétique uniforme, stationnaire et parallèle au champ de gravité. Des mesures thermiques ont permis de suivre l'évolution des distributions de température dans le temps. Ces expériences ont été conduites pour différentes valeurs de la surchauffe, en absence et en présence de champ magnétique. Une discussion, reliant les résultats cristallographiques aux topographies des champs de température, est présentée.

EINFLUSS DER MAGNETISCH GEDÄMPFTEN KONVEKTION BEI DER ERSTARRUNG VON METALLEN UND LEGIERUNGEN

Zusammenfassung—Die Rolle der natürlichen gedämpften Konvektion bei der temperaturbedingten Erstarrung von Zinn- und Aluminiumlegierungen in einer torusförmigen Gießform wurde untersucht. Die Dämpfung wurde durch ein stationäres und gleichmäßiges Magnetfeld (parallel zum Gravitationsfeld) bewirkt. Mit den Temperaturmessungen konnten sowohl der Erstarrungsverlauf als auch die zeitabhängige Temperaturverteilung in der Schmelze beobachtet werden. Diese Versuche wurden bei verschiedenen Überhitzungen mit und ohne Magnetfeld durchgeführt. Die kristallographischen Einflüsse auf die Gestalt des Temperaturfeldes werden diskutiert.

ВЛИЯНИЕ МАГНИТНОГО ПОЛЯ НА УПРАВЛЕНИЕ ПРОЦЕССОМ ЗАТВЕРДЕВАНИЯ МЕТАЛЛОВ И СПЛАВОВ

Аннотация—Исследовалась роль естественной и затухающей МГД-конвекции в процессе регулируемого затвердевания сплавов олова и алюминия в тороидальном канале. Подавление конвекции осуществлялось наложением стационарного и однородного магнитного поля, ориентированного параллельно полю сил тяжести. Измерения температур позволили проследить как за продвижением фронта затвердевания, так и за временным изменением распределения температур в объеме расплава. Эксперименты проводились при различных степенях перегрева расплава с магнитным полем и без него. Проведено обсуждение результатов кристаллографической диагностики температурных полей.